



PAPER

Nanomechanical-ferroelastics behavior, and the low-temperature ferroelectric manifestation of BiMnO_3 thin films

To cite this article: G V Umoh *et al* 2024 *Phys. Scr.* **99** 035962

View the [article online](#) for updates and enhancements.

You may also like

- [Role of O defects at the \$\text{BiMnO}_3/\text{SrTiO}_3\$ interface](#)
J Jilili, F Cossu and U Schwingenschlögl
- [Local distortions in multiferroic \$\text{BiMnO}_3\$ as a function of doping](#)
Alexei A Belik
- [Ac susceptibility studies of multiferroic \$\text{BiMnO}_3\$ and solid solutions between \$\text{BiMnO}_3\$ and \$\text{BiScO}_3\$](#)
Alexei A Belik and Eiji Takayama-Muromachi



PAPER

Nanomechanical-ferroelastics behavior, and the low-temperature ferroelectric manifestation of BiMnO₃ thin filmsRECEIVED
4 August 2023REVISED
29 January 2024ACCEPTED FOR PUBLICATION
19 February 2024PUBLISHED
28 February 2024G V Umoh¹, A E Gómez-Ovalle², M P Cruz³ , J E Leal-Pérez⁴ , Okure U Obot⁵, Héctor Urzola Berrio⁶, Raúl Herrera-Basurto⁷, F Mercader-Trejo⁸ and A Hurtado-Macias^{1,*} ¹ Centro de Investigación en Materiales Avanzados, S.C. (CIMAV) and Laboratorio Nacional de Nanotecnología (NANOTECH), Miguel de Cervantes 120, Complejo Industrial Chihuahua C.P. 31136, Chihuahua, Chih., Mexico² Department of Materials Science and Engineering, Texas A&M University, College Station, TX 77483, Mexico³ Centro de Nanociencias y Nanotecnología, Universidad Nacional Autónoma de México, Ensenada, Mexico⁴ Universidad Autónoma de Sinaloa. Gral. Ángel Flores S/N, Fracc. Las Fuentes, Los Mochis, Sin., C.P. 81223, Mexico⁵ University of Uyo, 520003, Nigeria⁶ Centro de Investigación e Innovación Corporación Universitaria Antonio de José de Sucre, Carretera 21 25-59, Sincelejo, Colombia⁷ Centro de Ingeniería y Desarrollo Industrial, Santiago de Querétaro 76130, Qro, Mexico⁸ Universidad Politécnica de Santa Rosa Jáuregui, Querétaro, Mexico

* Author to whom any correspondence should be addressed.

E-mail: abel.hurtado@cimav.edu.mx**Keywords:** BiMnO₃-thin-film, mechanical-properties, finite-element, ferroelectricity, ferroelastic behavior**Abstract**

Ferroelastic-nanomechanical behavior of BiMnO₃ thin films on (100) Nb-doped SrTiO₃ substrate is studied at the nanoscale, for the first time using the theories of depth sensing indentation and finite element analysis. This was to understand the redirection of polarization in ferroelastic behavior using piezoelectric direct effect and applying a controlled local force by nanoindentation. The values of the nanomechanical properties Young's modulus (E), hardness (H), and Stiffness (S) were measured to be $E = 142 \pm 3$ GPa, $H = 8 \pm 0.2$ GPa, and $S = 44072 \pm 45$ N m⁻¹ respectively. Using the experimental mechanical properties, a finite element analysis was carried out to understand the relationship between the irreversible work versus depth curve and plastic-deformation evolution of the thin film-interface-substrate system, associated with the pop-in observed. Von Mises stress maps are presented to clearly illustrate the deformations, mechanical failures, and influences between the BiMnO₃ film and the SrTiO₃ Substrate. The ferroelastic range for BiMnO₃ material was observed between 0 to 12 nm, and the yield strength was $Y = 2.6 \pm 0.7$ GPa. The ferroelectric properties through hysteresis curves were evaluated at two different temperatures of 200 K and 300 K in order to observe the effect of polarization with temperature. Providing better polarization performance at lower temperatures; $P_s = 9.14 \pm 0.01$ (μ C cm⁻²), $P_r = 2.23 \pm 0.02$ (μ C cm⁻²) and $H_c = 0.77$ kV cm⁻¹.

1. Introduction

Multiferroics thin film of BiMnO₃, possess a strong intrinsic coupling between the strain and spontaneous polarization. Its application is found in high-density non-volatile memories, actuators, spintronic devices, and piezoelectric sensors [1–4]. The electromechanical coupling in this material allows for the conversion efficiency of mechanical to electrical energy or vice versa. This switching behavior is crucial to material properties, including piezoelectric response in ferroelectrics, dielectric, and magnetoelectric coupling in multiferroic [1, 5, 6]. Several reports on multiferroic, basically mentioned electric field, and magnetic field, nullifying the role of ferroelasticity. However, ferroelasticity and strain tend to proffer much of the coupling between ferroelectric and ferromagnetic properties [7–9]. Polycrystalline BiMnO₃ at room-temperature is reported to show interesting electrical and magnetic properties [10, 11]. The first crystallographic studies of BiMnO₃, the structure was refined in a non-centrosymmetric space group, $C2$, which allows ferroelectricity [12]. Furthermore, according to studies, ferroelectricity exists in systems with one of two perovskite-based

polymorphs, depending on sintering temperature, viz.: monoclinic, and hexagonal [13, 14]. First-principles calculations suggested appropriate ferroelectricity associated with the highly polarized $6s^2$ character of Bi^{3+} (lone pairs), which is associated with the John-Teller (JT) structural distortion, with its parameter as stated $\Delta = \left(\frac{1}{6}\right) \sum_{n=1,6} \left[\left(\bar{x}d_n - \left\langle \frac{\bar{x}d}{\bar{x}d} \right\rangle \right) \right]^2$ of 37.2×10^{-4} and 51.3×10^{-4} . Where $\bar{x}d$ is the average of the (Mn–O bond length) [15].

In addition, Different space groups in monoclinic BiMnO_3 give diverse results from the optical studies of its phonon spectrum in Raman spectroscopy. Raman modes predicted by group theory analysis give (Γ_{Raman} , $C2 = 29A + 31B$) = 57 phonons for the $C2$ structure of BiMnO_3 , one A, and two B vibrations are acoustic. Both infrared (IR) and Raman active, Space group $C2/c$, has a representation of $14A_g + 14A_u + 16B_g + 16B_u$ where this is due to the inversion symmetry, all of the A_g and B_g modes are Raman active, the 13 A_u and 14 B_u modes are infrared active, while the remaining ones are acoustic [12, 16].

In this work, it is reported only as a part of the research study of Glory Umoh's doctoral thesis [17], which is a completely new work. Thin films were grown by radio-frequency magnetron sputtering technique on (150 nm) thickness, on Nb-doped SrTiO_3 substrate, and was annealed at 973 K for 7 h. P-E hysteresis loops ($K = 200$ and 300) were conducted. The P-E plot at $K = 200$ shows clear hysteresis, confirming the ferroelectric nature of the polycrystalline multiferroic thin film. It is accompanied by reduced remanent polarization ($Pr \approx 4.0 \mu\text{C cm}^{-2}$) and an increased electric field ($E = 22.0 \text{ kV cm}^{-1}$), which is advantageous for storage performance in electronic devices. On the other hand, an analysis of the piezoresponse was carried out in this multiferroic material using Piezoresponse Force Microscopy (PFM) in order to verify that it has ferroelectric-piezoelectric properties.

Ferroelastic behavior through force-penetration depth, based on Oliver–Pharr's indentation method was investigated. Ferroelastic behavior, elastic modulus (E), stiffness (S), and hardness (H) were measured, and the curves give a better understanding of the different mechanical behaviors of BiMnO_3 . An interesting phenomenon ('pop-in') in the load-displacement curve was observed at a specific depth (14–40 nm) of the thin film. Finite element (FE) modeling, along with the experimental characterization methods in the indentation test, to analyze features that were not directly available during the experimental evaluation. Physical properties of ferroelectric polarization at different temperatures were also measured. This report is envisioned to facilitate the application of BiMnO_3 in microelectromechanical systems devices.

2. Experimental details

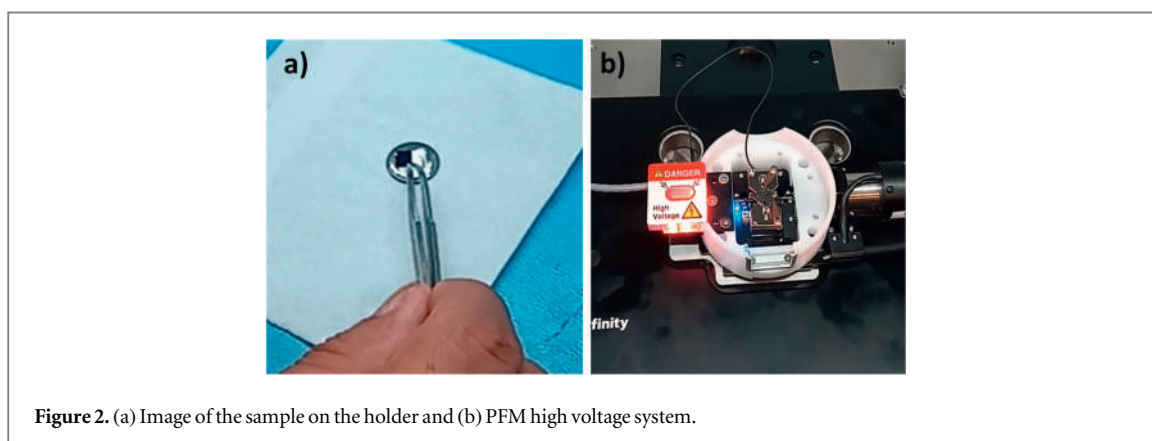
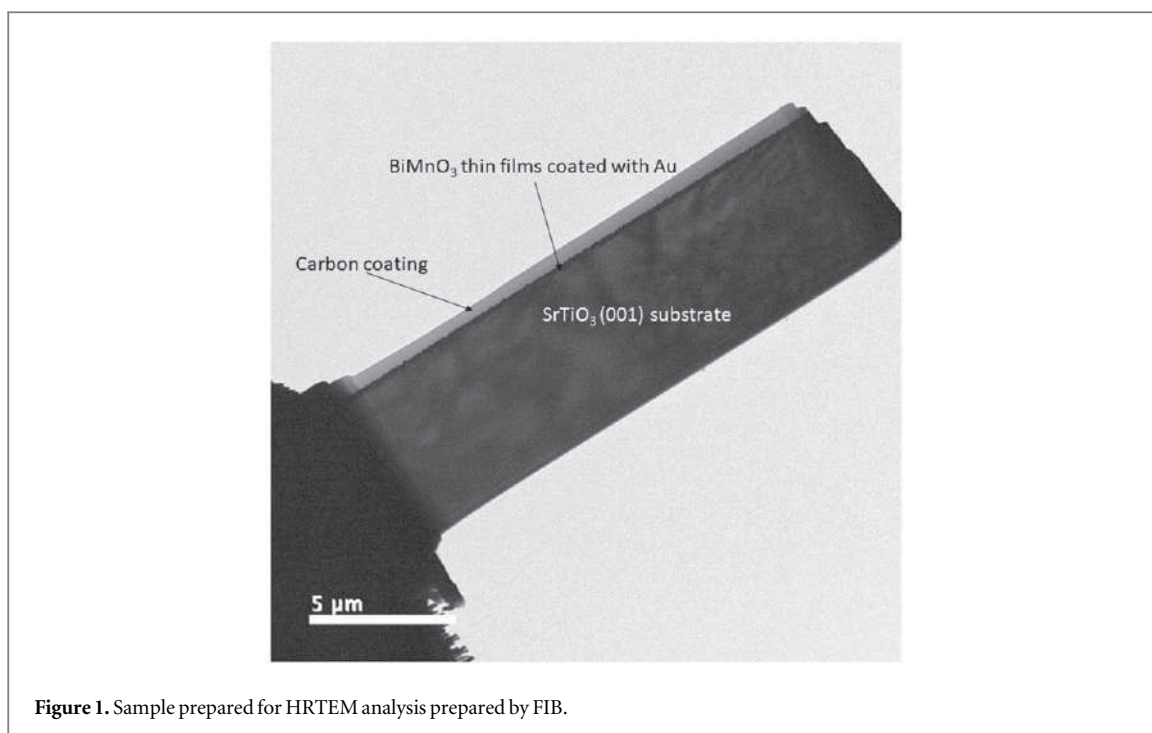
As previously reported, with details elsewhere [18], BiMnO_3 thin films were obtained via radio-frequency magnetron sputtering. Nb-doped SrTiO_3 (100) single crystal was used as the substrate for the growth of BiMnO_3 thin film, due to its smaller lattice mismatched with BiMnO_3 . A ($\sqrt{2} \times \sqrt{2}$) $R45^\circ$ fictitious cell of SrTiO_3 (100) with a lattice constant of 5.52 Å. This being a reasonable value reflected on an induced deformation at the interface along the $b\text{BMO}$ direction. The optimum parameters used for growing the BiMnO_3 films were: (1) sputtering chamber was evacuated to a base pressure of 5×10^{-8} Torr; (2) radio frequency power of 60 W; (3), deposition temperature of $873 \pm 5\text{K}$; (4) was found to be the optimized temperature to obtain the composition of BiMnO_3 at a deposition rate was of 1.1 nm/min. Substrate rotation speed of 3 RPM; (5) Ar flow rate of 13 sccm providing a chamber pressure, during film growth, of 3×10^{-3} Torr. After film growth, *ex situ* thermal treatment was carried out using a tubular furnace with a rich O_2 atmosphere, flow rate 20 sccm, and Ar flow rate of 200 sccm.

2.1. Microstructural characterization

X-ray diffraction (XRD) patterns in Bragg–Brentano geometry were collected in (XRD-Philips X'Pert MPD) at room temperature. The data were acquired from 15° to 75° using a step size of 0.02° , and a scan speed of 0.22 s per step. Additionally, the microstructure of BiMnO_3 was characterized by high-resolution transmission electron microscopy (HR-TEM) with a JEOL TEM-2200FS + Cs microscope operated at 200 kV.

The preparation of the sample for HRTEM was by focused ion beam system (FIB) using a model JEM-9320FIB equipment, to have the appropriate dimensions and good effectiveness in the transmission of electrons. Figure 1 shows a SEM image of the sample prepared for HRTEM analysis, showing the architecture and dimensions of the sample device used. In the preparation of the sample, it must be coated with Au to be able to manipulate it in FIB and carbon to protect the sample.

On the other hand, Raman spectroscopy was performed using Micro Raman Labram HR VIS-633 Horiba with an Olympus microscope. The spectra were acquired between 180 and 1050 cm^{-1} using a He–Ne laser with a 632.8 nm wavelength. The power and spot diameter were 14 mW and $15 \mu\text{m}$, respectively.



2.2. Ferroelectrics and piezoelectric details characterization

Ferroelectric characterization was carried out at 200 and 300 K, circular dots of platinum electrodes of about 50–100 μm diameter were painted in circular faces and annealed at 873 K for 30 min for the ferroelectric measurements. The AC voltage was set at 0.5 V with a drive frequency of 100 Hz. The temperature controller and cooling system used for ferroelectric measurements was a Cryodyne 22C model with LTS series. The system employed for the data collection during the P-E characterization was the precision LC analyzer with the VISION 5.6.0 software and an RT66 test system from Radiant Technologies Inc.

2.3. Experimental details of the piezoelectric force microscopy (PFM) method characterization

The electrical domains of BiMnO_3 thin film were investigated by piezoelectric force microscopy (PFM), using an atomic force microscope (AFM) model Asylum Research Infinity 3D, with 2 internal lock-ins and an amplifier. The sample was placed in the AFM holder, and was fixed with silver paint, as shown in figure 2(a)). This was to avoid electrostatic charges on the surface interfering with the measurement. The sample was placed inside the PFM high voltage system and connected to the high voltage cable that interacted with the sample through the tip in the PFM measurement (figure 2(b)).

The measurement zone is determined, and a scan is carried out on the $2.5 \times 2.5 \mu\text{m}$ sample in contact mode with the optimal parameters. The AC voltage amplitude of 5 V_{pk-pk} and a drive frequency of 275 kHz below the resonance frequency Hz, of the cantilever were applied between the bottom electrodes (Pt substrate) and Pt/Ir tip during the acquisition of the PFM image.

To obtain local polarizations from piezo-hysteresis loops, voltages of -20 to $20 V_{pk-pk}$ were applied in dual AC resonance tracking (DART) in the Switching Spectroscopy PFM (SS-PFM) technique. The PFM measures the BiMnO₃ thin film topography along with its mechanical stress, in response to the application of electrical voltage.

$$V_{tip} = V_{dc} + V_{ac} \sin(\omega t) \quad (1)$$

Where V_{dc} and V_{ac} correspond to the dc and ac voltages, respectively, and ω to the oscillation frequency. The electric field yields piezoelectric stress in the material that causes displacement in the cantilever, as a consequence of the indirect piezoelectric effect [19, 20].

$$z = z_{dc} + A(\omega, V_{ac}, V_{dc}) \sin(\omega t + \varphi) \quad (2)$$

If the applied voltage is at a frequency below the contact resonance of the cantilever, the equation is given by:

$$z = d_{33} V_{dc} + d_{33} V_{ac} \sin(\omega t + \varphi), \quad (3)$$

2.4. Nanomechanical characterization by nanoindentation

To measure the nanomechanical properties of the BiMnO₃, a diamond Berkovich indenter was used for all measurements. The hardness, elastic modulus, and stiffness were evaluated using standard procedures of the Oliver and Pharr method with controlled cycles [1, 2, 21]. The stiffness was calculated by the Sneddon equation as follows:

$$S = 2\beta \sqrt{\frac{A}{\pi}} E_r \quad (1a)$$

where β is a constant that depends on the geometry of the indenter ($\beta = 1.034$ for a Berkovich indenter), E_r is the reduced elastic modulus, which accounts for the fact that elastic deformation occurs in both the sample and the indenter, and A is the contact area that is a function of the penetration depth or displacement (h) [22]. The elastic modulus, E was calculated by considering the compliance of the specimen and the indenter tip combined in series, by the following equation:

$$E = \frac{1 - \nu^2}{\left(\frac{1}{E_r} - \frac{1 - \nu_i^2}{E_i}\right)} \quad (2a)$$

Where E_p , E , ν_p , and ν are elastic modulus and Poisson's ratio of diamond indenter and specimen respectively. For the diamond indenter $E_i = 1140$ GPa and $\nu_i = 0.07$ are used (G200 Agilent manual, Agilent technology USA). The hardness (H) was calculated using the equation:

$$H = \frac{P_{max}}{A(h)} \quad (3a)$$

Furthermore, the analysis depth was set between 5 to 10% of the total thickness of the film to avoid the influence of the hardness of the substrate.

The maximum load used was 5 mN, with a time of 10 s for loading and 10 s for unloading during nanoindentation. Peak hold time of 1 s was used before unloading. The Poisson's coefficient of $\nu = 0.20$ was employed before evaluation, the coatings of the nanoindenter were calibrated using a standard fused silica sample. Tests parameters of the area function were: $C_0 = 24.07$, $C_1 = -182.16$, $C_2 = 6831.20$, $C_3 = -25411.22$, and $C_5 = 18732.10$.

2.5. Modeling details

In the numerical modeling for the understanding of plastic deformation of the BiMnO₃ (110nm thickness)/SrTiO₃ (10 μ m) thin film system. The software used was Abaqus/standard 2021 to simulate nanomechanical behavior. The finite element model of the contact mechanics is constructed considering the elastic-plastic (elastic, perfectly plastic) behavior of the thin film. The Berkovich indenter was modelled like an elastic material ($E = 1000$ GPa). This is because the indenter is not permanently or plastically deformed. The in-plane BiMnO₃/SrTiO₃ thin film dimensions are sufficiently large to eliminate any border effects on the indentation stress/deformation fields. Linear, 3D, 8-noded brick elements with reduced integration, and hourglass control were employed to discretize the system. The elastic modulus (E) was obtained from the analysis of the BiMnO₃ thin film nanoindentation test data. The yield stress (σ_y) was calculated from the hardness (H) obtained by nanoindentation and the Tabor relationship ($\sigma_y = H/3$). Ten finite element models were constructed with 10, 20, 30, 40, 50, 60, 70, 80, 90, and 100 elements at the contact radius (half of the contact). The element sizes were 0.406, 0.313, 0.230, 0.214, 0.210, 0.205, 0.198, 0.197, and 0.196 μ m. The contact area between the indenter and the system surface was utilized as a measure to establish the independence of the finite element predictions with

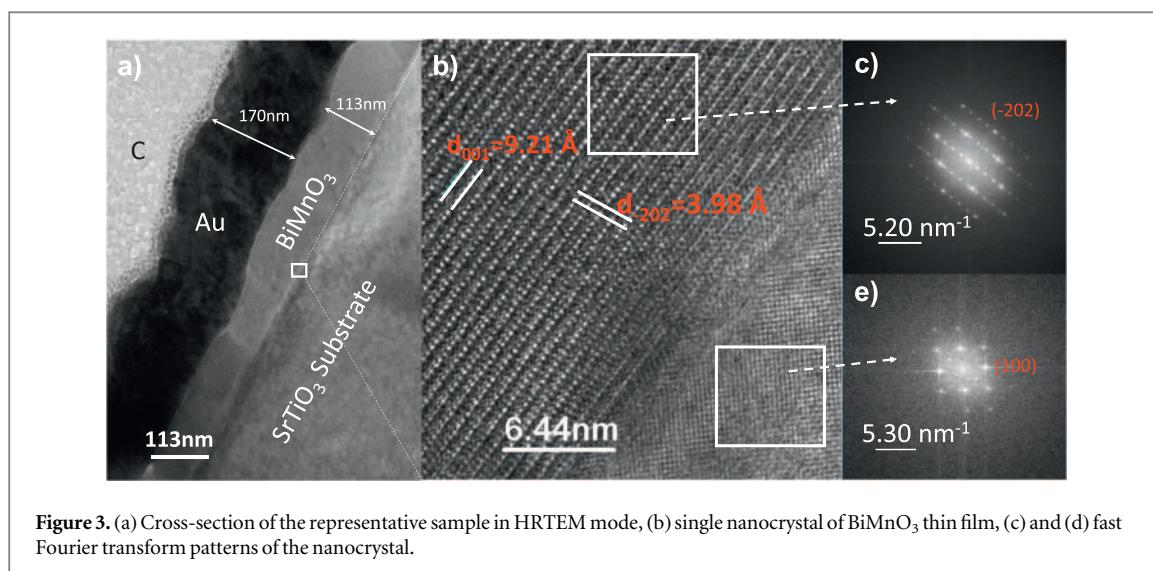


Figure 3. (a) Cross-section of the representative sample in HRTEM mode, (b) single nanocrystal of BiMnO₃ thin film, (c) and (d) fast Fourier transform patterns of the nanocrystal.

the mesh size. An element size of $0.198 \mu\text{m}$ and 80 elements in contact represent a good balance between accuracy and computational cost. The simulations discussed in figure 5 were conducted utilizing this mesh size.

3. Results and discussion

The high-resolution transmission electron microscopy technique (HRTEM) was required to complement the structural characterization and the integrity of the interface at nanometer resolution. Figure 3(a), is the representative sample of the cross-section of the film with a scale of $113 \pm 3 \text{ nm}$, showing the BiMnO₃ thin film, single crystal SrTiO₃ (001) substrate. From these images, the film thickness was determined to be approximately $113 \pm 3 \text{ nm}$, the Au-capped with thickness of $140 \pm 4 \text{ nm}$ and carbon layer of $170 \pm 5 \text{ nm}$. The interface between the film and substrate is well-defined, and the nanocrystals in the Raman spectra are verified, without any appreciable interdiffusion between the film and the substrates.

Figure 3(b) shows the interface of the nanocrystal represented with a white square region, where the interplanar distance of $d_{(110)} = 4.75 \text{ \AA}$, and $d_{(-201)} = 3.55 \text{ \AA}$ of the BiMnO₃ is observed. These planes and their respective indexing are with reference PDF card number: 01-089-4544. A comparison of the experimental HRTEM pattern and digital diffractogram of the planes were identified, as a monoclinic BiMnO₃ structure with a space group, C2. These results correspond well with the results obtained by Yokosawa *et al* [23]. Their crystalline parts are randomly oriented with respect to each other, which demonstrates their polycrystallinity with no indication of epitaxial layer formed. Figures 3(c) and (d) show the fast Fourier transform patterns in the marked squares in figure 3(b) representing the thin film and the SrTiO₃ substrate with planes along (-201) and (100) zone axis respectively. Analyzing the substrate using electron diffraction patterns, it is determined that it is a (100) plane with a cubic structure with spatial group Pm-3m according to the letter pdf00-035-0734.

Figure 4 shows the XRD pattern of a thin film synthesized at $873 \pm 5 \text{ K}$ and annealed at 973 K for 7 h. The diffraction peaks were indexed based on monoclinic-type C2, space group number 5 with crystallographic parameters; $a: 9.5323 \text{ \AA}$, $b: 5.6064 \text{ \AA}$, $c: 9.8536 \text{ \AA}$ agree to reference code: (PDF: 1-089-4544). All the peaks are associated with pure BiMnO₃, as was previously reported [18].

The most intense peak in the XRD pattern corresponds to the substrate SrTiO₃. The obtained diffraction pattern shows the formation of a pure structure without any secondary phase. Furthermore, BiMnO₃ was investigated by using Raman spectroscopy, which is known as a sensitive technique for detecting more subtle or phase structural rearrangements due to coupling phenomena in ABO₃ perovskites [19, 20]. Figure 5 presents Raman spectra measured at room-temperature spectra. The Raman spectrum (black dotted line) acquired in a range of $180\text{--}1050 \text{ cm}^{-1}$ is shown in figure 5.

Three prominent Raman bands emerged at 398.1 , 620.8 , and 1009.2 cm^{-1} on this polycrystalline BiMnO₃ sample. Apart from the three intense bands, other strong peaks are located at 234.5 , 374.1 , 398.1 , 620.8 , 665.8 , 729.3 , and 1009.2 cm^{-1} , their respective oscillation modes (TO) and longitudinal (LO), are illustrated in table 1. The most intense band at 398.1 cm^{-1} belongs to Ag symmetry of transverse optical (TO) phonon mode [Ag, (TO)]. The second intense and broad band is located near 374.1 cm^{-1} ; this feature is associated with Bg (TO) phonon [22, 24].

The sharp low intensity band near 620.8 cm^{-1} is associated with Bu symmetry of longitudinal optical (LO) phonon mode [Bu, (LO)], and high frequency band near 1009.2 cm^{-1} is related to Ag, (LO) phonons. These

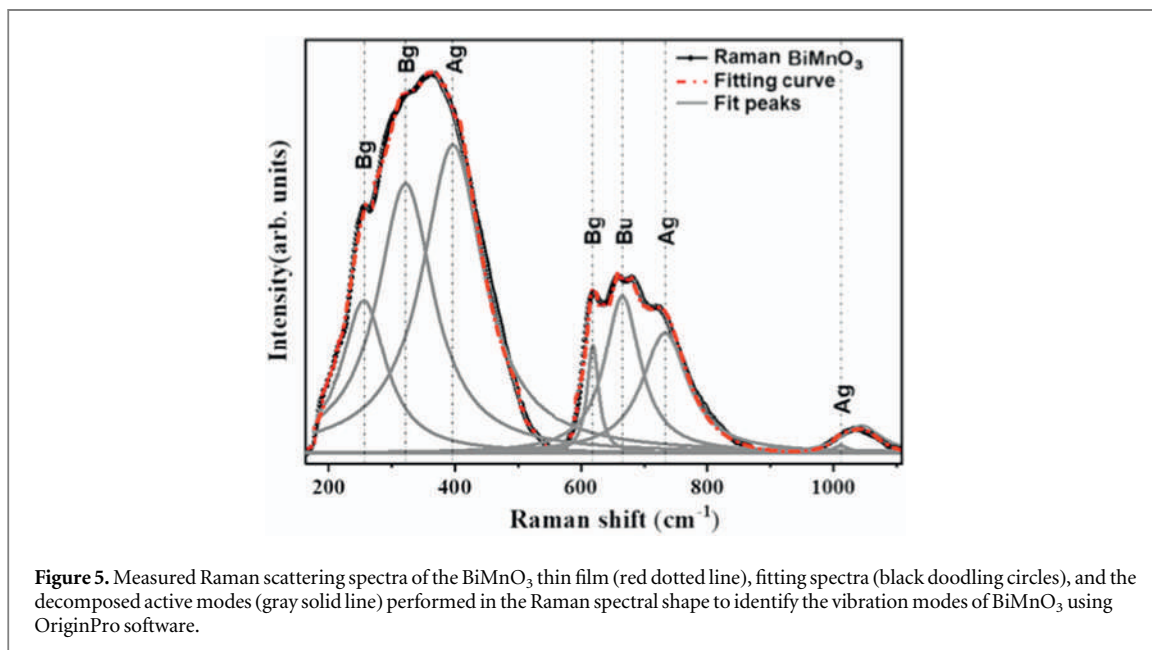
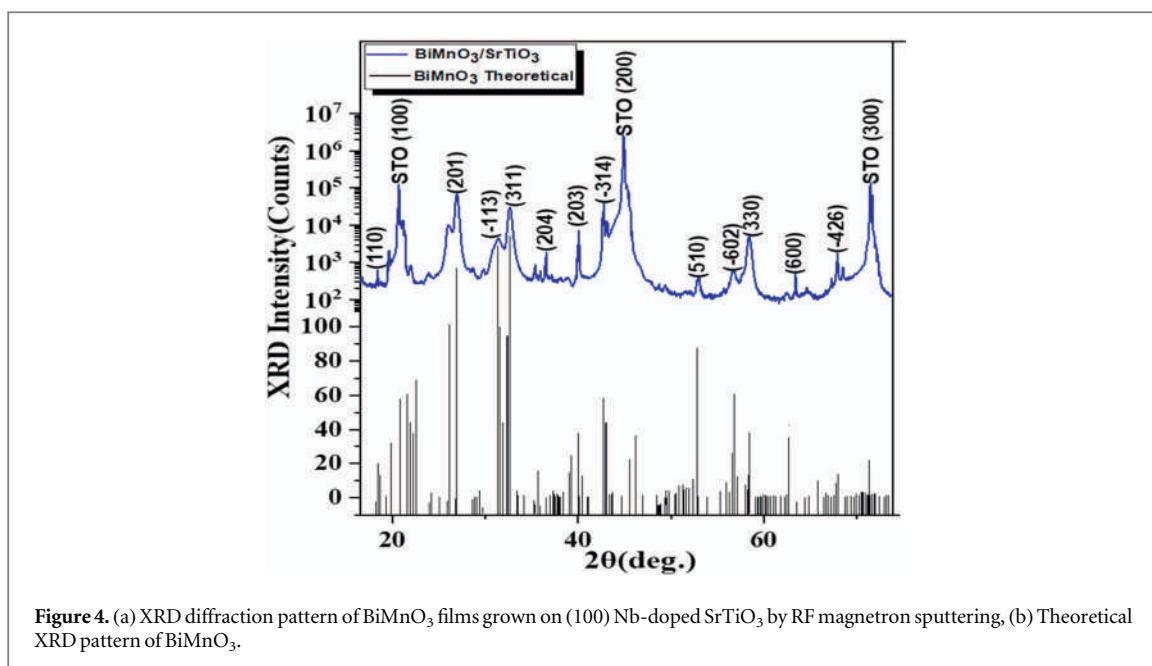


Table 1. Raman frequencies of IR, and raman active modes in the BiMnO₃ thin film.

Type	cm ⁻¹	IR
TO	234.5	Bg
TO	374.1	Ag
TO	398.1	Ag
LO	620.8	Bg
TO	665.8	Ag
TO	729.3	Bg
LO	1009.2	Ag

bands are characteristic for BiMnO₃ ferroelectric phase with monoclinic symmetry [12, 25]. The peaks at 260 and 1009.2 cm⁻¹ can be attributed to the lattice and stretching vibrations of the Mn–O bond. According to the Lorentz equation in OriginPro software [26] the deconvolution peaks of BiMnO₃ sum up to 52, close to that of

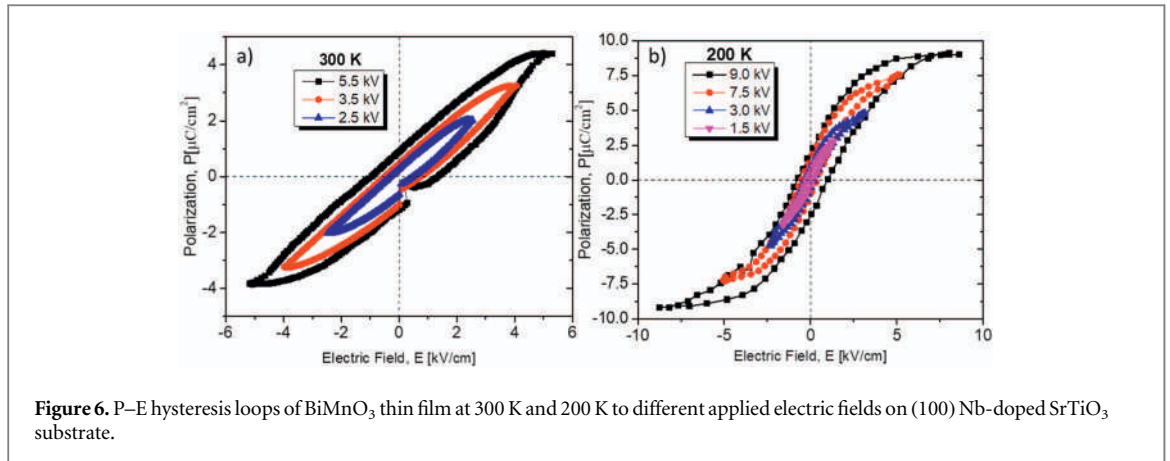


Figure 6. P–E hysteresis loops of BiMnO₃ thin film at 300 K and 200 K to different applied electric fields on (100) Nb-doped SrTiO₃ substrate.

the calculated 57 phonons [12, 16], for the monoclinic phase reported elsewhere with the C_2 space group (C_2^3 No. 5) [18]. The factor group analysis of all phonons with Γ point in Brillouin-zone center predicts the following: $\Gamma_{C_2} = 29A(z, x^2, y^2, z^2, xy) + 31B(x, y, yz, xz)$ [12, 27], where A and B denote acoustic vibrations. In the bracket shows the Raman, and IR activity respectively. The Raman modes were obtained by fitting the experimental spectra (black doodling circles), peak fitting curve (red solid line), and fit peak (gray solid line) with Gaussian–Lorentzian shape components according to the Raman active modes [28, 29]. It is important to note that, the observed bands corresponds to several phonons because frequencies of the modes are relatively close. Raman activity can arise due to several reasons, such as: grain boundaries, intergrain stresses, and phonon anomalies which are common for some multiferroics materials, BiMnO₃, HoMnO₃, LuMnO₃, and YMnO₃ [30]. To our knowledge there is no report on C_2 space group of BiMnO₃ to compare the modes and frequencies to our experimental result.

Ferroelectric hysteresis loops of the BiMnO₃ thin films at 300 K and 200 K are shown in figure 6(a) and (b) with different applied electric fields respectively. The figures establish the ferroelectric behaviour of the BiMnO₃ thin films displaying nearly saturated at 300 K and saturated hysteresis loops at 200 K.

Both representative samples show distinct hysteresis characteristics with different applied electric fields, due to the temperature difference. In Figure 6(a) the value of polarization is high ($P_s \approx 4.06 \mu\text{C cm}^{-2}$ at $\approx 5.3 \text{ kV cm}^{-1}$); with an elliptical P-E shape, this proves that the electric field is sufficient to switch the domains. Likewise, the report of M Grizalez *et al* [31]. At $T = 200 \text{ K}$, displays a typical ferroelectric hysteresis loop, the increase of electric field may be due to the long-rang interaction of structural dipoles on cooling, as shown in figure 6(b). It is difficult to have good ferroelectric behaviour in perovskite materials at a temperature higher than 300 K and below 100 K [32, 33]. We suggest that this behaviour may be due to change in the structural dipoles' orientation of the BiMnO₃ films. The other physical properties are presented in the table 2.

Moreover, in order to corroborate the ferroelectricity through the phase hysteresis and electrical displacement curves, as well as the ferroelectric polarization orientation in the multiferroic samples, the PFM results at room temperature are presented. Figure 7(a) shows the contact mode topography of a $2.5 \mu\text{m} \times 2.5 \mu\text{m}$ scan of a representative sample of the BiMnO₃ thin film, where the equiaxial grain structure with a size of $113 \pm 22 \text{ nm}$ can be observed. Figure 7(b) shows the PFM mode amplitude image of the ferroelectric domain structure of the representative sample. Figure 7(c) shows the phase signal, which shows the spontaneous orientation of the polarization, that is, how the orientation of the ferroelectric polarization is found in the sample.

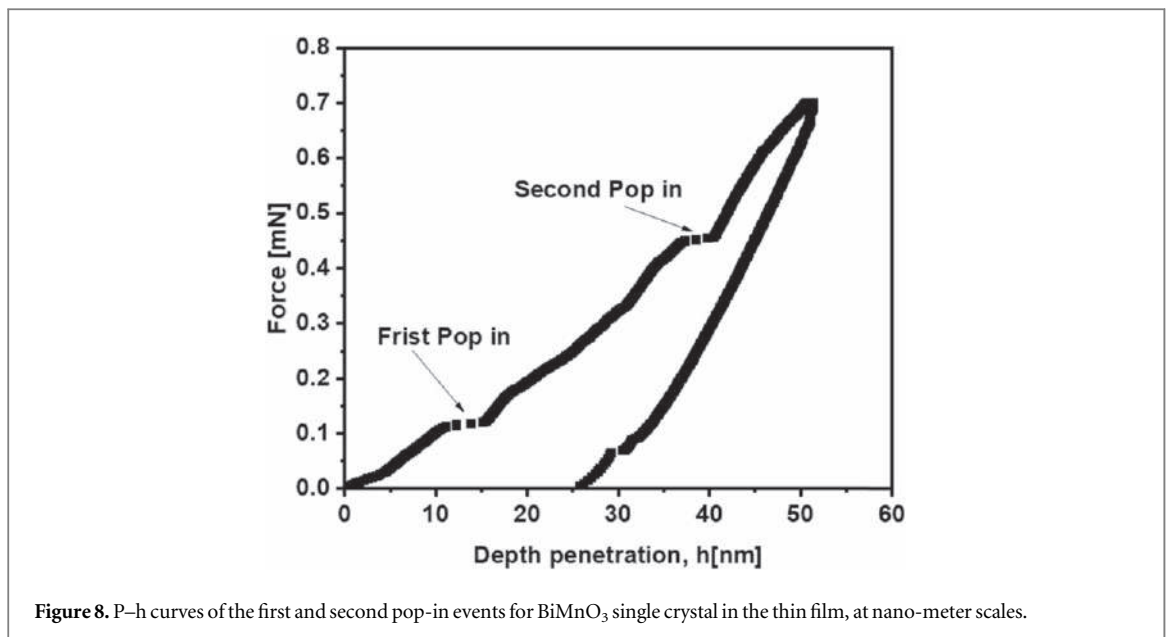
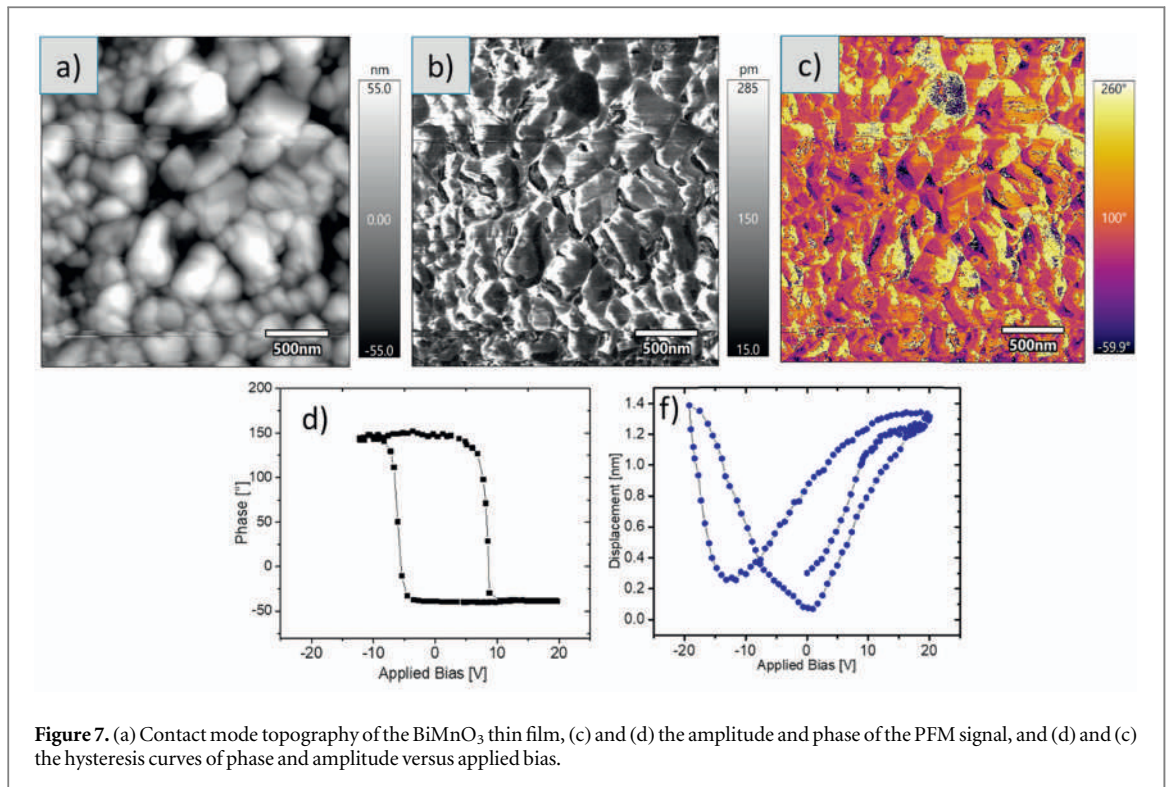
The SS-PFM results of the ferroelectric phase and electrical displacement hysteresis curves are shown in Figures 7(d) and (f) respectively. In figure 7(d) is clearly observed the redirection or switching of the ferroelectric domains caused by the applied electric field or the applied bias that was applied from -20 V to 20 V . A coercive voltage of 4 V was obtained by using the relation $(V_{c+} - V_{c-})/2$, where V_{c+} and V_{c-} are forward and reverse coercive bias voltages, respectively. Figure 7(f) shows how the ferroelastic displacement caused by the applied electric field originates, reaching a displacement of 1.39 nm .

Therefore, we can conclude that the BiMnO₃ film exhibits ferroelectric behavior compared to other similar BiMnO₃ materials that other researchers have investigated [34].

Figure 8 displays a characteristic load-depth penetration curve of a single crystal BiMnO₃ Thin film with the maximum penetration load of 0.7 mN and the loading/unloading rate of 0.58 mN s^{-1} . A first single sudden discontinuity (Frist, pop-in) in the load–displacement curve was observed at a specific depth ($0\text{--}14 \text{ nm}$) of the BiMnO₃ thin film.

Table 2. Ferroelectrics and nano-mechanical properties of BiMnO₃ Thin film.

Ferroelectrics properties					Nano-mechanical properties				
Temp. (K)	Applied Voltage (V)	Ps ($\mu\text{ C cm}^{-2}$)	Pr ($\mu\text{ C/cm}^2$)	Hc (kV cm^{-1})	h_{max} (nm)	Stiffness, S [Nm^{-1}]	Young modulus, E [GPa]	Hardness, H [GPa]	Yield Strength, Y
200	5	9.14 ± 0.01	2.23 ± 0.02	0.77	48 ± 0.2	44072 ± 45	142 ± 3	8 ± 0.2	2.6 ± 0.7
300	5	4.06 ± 0.02	0.62 ± 0.03	1.02					



The physical mechanism responsible for the ‘pop-in’ event in this thin film may be due to the interaction behavior of the threading dislocations during the mechanical deformation. Also, it is directly related to the yield point [35, 36]. Similarly, the second pop-in is normally attributed to failure of the material due to fractures [37, 38], or in the case of coatings on a substrate it could be the failure due to adhesion between the substrate and the film, this is clarified later in the simulation part. In other words, the elastoplastic transition is observed by a sudden penetration effect called pop-in. This sliding effect is related to the onset of permanent or plastic deformation due to the origin of the dislocations. Static indentation hardness tests usually imply the application of load to a spherical or pyramidal indenter. Experiments show that the hardness between the indenter and the sample is directly proportional to the yield of the material, and can be expressed as; $H \approx CY$, where Y is the yield, or flow stress, of the material and C is called the ‘constraint factor,’ the value of which depends upon the type of sample and indenter geometry. Invoking the Tresca shear stress criterion, gives: $H = Y(1 + \alpha)$, (taken $\alpha = 70^\circ$ to Berkovich indenter), therefore $C = (1 + \alpha)$, and with the von Mises criterion gives $C \approx 3$ [36, 39]. Therefore, the

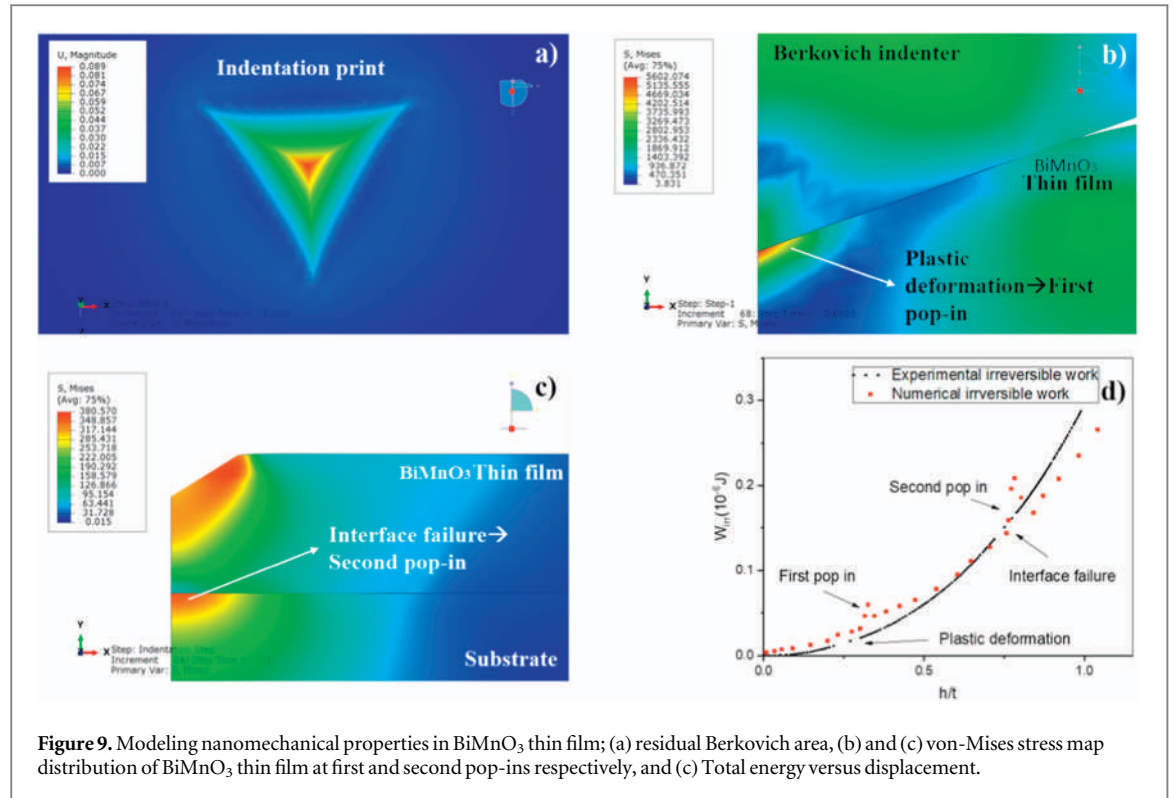


Figure 9. Modeling nanomechanical properties in BiMnO₃ thin film; (a) residual Berkovich area, (b) and (c) von-Mises stress map distribution of BiMnO₃ thin film at first and second pop-ins respectively, and (c) Total energy versus displacement.

yield point value for the monoclinic BiMnO₃ films is $Y = 2.6 \pm 0.7$ GPa. According to the Oliver-Pharr method [40], stiffness, hardness, and elastic modulus measured for the BiMnO₃ Thin films were, $S = 44072 \pm 45$ N m⁻¹, $H = 8 \pm 0.2$ GPa and $E = 142 \pm 3$ GPa respectively. The mechanical properties are presented in table 2. The thin film was subjected to an elastoplastic deformation. Thus, part of the total energy involved in the nanoindentation test is recovered as elastic energy, while the other part associated with the plastic deformation of the material during the indentation is dissipated as plastic energy.

The area below each of the loading curves (total energy applied) and unloading curves (elastic energy) make it possible to determine the percentage of plastic energy dissipated for the sample [41–43]. Moreover, another way to visualize the interval of the ferroelastic behavior is through the load penetration curve of figure 8. In this curve the first elastic behavior is delimited by the first penetration values and the yield limit Y , which is the ferroelastic behavior where the redirection of domains, either by the direct or indirect effect as some other authors have visualized [44, 45]. Therefore, it is important to visualize this ferroelastic behavior to see the performance of the piezoelectricity in an indirect way. In this case, the ferroelastic range for the BiMnO₃ material in thin film form is between 0 to 14 nm of the curve depth penetration delimited by the yield strength, $Y = 2.6 \pm 0.7$ GPa.

Due to experimental limitations in creating different depths of penetration in the BiMnO₃/SrTiO₃ substrate, a simulation of the mechanical properties by finite element is a key candidate for studying these systems, as shown in figure 9, where the different behaviors of von Mises stress map distribution at different depths of penetration in the BiMnO₃ film are clearly observed. Figure 9(a) demonstrates the Berkovich-type residual area image, which was modeled by finite element, using the experimental load-displacement curve.

This figure shows that there is no crack around this residual area as in other report on similar ferroelectrics material [37, 38]. Therefore, we can say that the second pop-in of the mechanical load-penetration behavior of figure 8, does not correspond to fracture in the BiMnO₃ thin film, but to the failure of the interaction between the BiMnO₃ film and the SrTiO₃ single crystal substrate or abrupt change from passing to the substrate, called an interference failure. Figure 9(b) displays the von Mises stress map distribution at the first pop-in, where propagation to the deformation has already started, by means of the dislocations or twins in the BiMnO₃ thin film. On the other hand, figure 9(c) illustrates the von Misses stress maps of the second pop-in, which corresponds to the failure mentioned above due to the delamination between the BiMnO₃ film and the SrTiO₃ substrate. Figure 9(d) shows the curve of irreversible energy involved (W_{irre}) versus displacement or depth of penetration normalized with the thickness of the thin film (h/t). A sudden marked are seen in the curve segments at 0.05 and 0.22 W_{irre} (10^{-5} J) of about 0.03 and 0.9 h/t respectively. This irreversibility, is due to the strain induced under pressure, and provides independent evidence for the onset of plastic deformation and interface failure of the BiMnO₃ thin film, and SrTiO₃ substrate of the first and second pop-in respectively. In other words,

thermodynamically the energies involved in the irreversible changes caused by the plastic deformation and the failures between the film and the substrate are clearly shown in this curve.

4. Conclusion

Through Raman analysis, it was possible to identify the monoclinic phase with the C2 space group according to the vibrational modes, identified by the transverse optical (TO) and longitudinal optical (LO) oscillation modes corresponding to polycrystalline BiMnO₃ thin film. Clear interfaces between the thin film and substrate was observed in the HRTEM results, and there is no preferential orientation or epitaxy between the (100) Nb-doped SrTiO₃ substrate and the polycrystalline BiMnO₃ thin film. This study for the first time systematically investigated the ferroelastics behavior, and the low-temperature ferroelectric manifestation between the BiMnO₃ thin film and the SrTiO₃ substrate. The Ferroelectric properties of BiMnO₃ were found to improve at 200 K. The pop-in characteristics and mechanical properties of BiMnO₃ were methodically studied by Oliver and Pharr method in nanoindentation. The nanomechanical properties were evaluated, such as: elastic modulus, hardness, and stiffness, with obtained values of $S = 44072 \pm 45 \text{ N m}^{-1}$, $E = 142 \pm 3 \text{ GPa}$, and $H = 8 \pm 0.2 \text{ GPa}$ respectively. The ferroelastic range for the BiMnO₃ material was observed between 0 to 12 nm, and the yield strength, was found to be $Y = 2.6 \pm 0.7 \text{ GPa}$. Using a finite element, the von Mises stress maps distribution of the BiMnO₃ thin film and SrTiO₃ substrate were determined. Therefore, the irreversibility is due to the strain induced under pressure and provides independent evidence of beginning plastic deformation and interface failure of the BiMnO₃ thin film and (100) Nb-doped SrTiO₃ substrate, of the first and second pop-in respectively. Values deduced from the mechanical and ferroelectric measurement of BiMnO₃ thin film revealed that BiMnO₃ thin films are attractive materials for energy harvesting, spintronics, spin valves, sensor applications, and microelectromechanical systems devices.

Acknowledgments

The authors thank and acknowledge CONAHCYT (grant number 954265) and the members of staff at the Centro de Investigacion en Materiales Avanzados, S C, Mexico, for the characterization and analysis. Roberto Talamantes and Gerardo Resendiz, for technical support in sample preparation by FIB.

Data availability statement

No new data were created or analysed in this study.

ORCID iDs

M P Cruz  <https://orcid.org/0000-0002-8407-5741>

J E Leal-Pérez  <https://orcid.org/0000-0002-6215-1109>

A Hurtado-Macias  <https://orcid.org/0000-0002-0406-3776>

References

- [1] Latalski J, Kowalczyk M and Warminski J 2022 Nonlinear electro-elastic dynamics of a hub–cantilever bimorph rotor structure *Int. J. Mech. Sci.* **222** 107195
- [2] Zhou D, Kamlah M and Munz D 2005 Effects of bias electric fields on the non-linear ferroelastic behavior of soft lead zirconate titanate piezoceramics *J. Am. Ceram. Soc.* **88** 867–74
- [3] Jin C *et al* 2021 Super-flexible freestanding BiMnO₃ membranes with stable ferroelectricity and ferromagnetism *Adv. Sci.* **8** 1–9
- [4] Sun B and Li C M 2015 Light-controlled resistive switching memory of multiferroic BiMnO₃ nanowire arrays *Phys. Chem. Chem. Phys.* **17** 6718–21
- [5] Kajiwara I, Kitabatake S, Hosoya N and Maeda S 2019 Design of dielectric elastomer actuators for vibration control at high frequencies *Int. J. Mech. Sci.* **157–158** 849–57
- [6] Jin C *et al* 2021 Ferroelectricity and ferromagnetism achieved via adjusting dimensionality in BiFeO₃/BiMnO₃ superlattices *ACS Appl. Mater. Interfaces* **13** 41315–22
- [7] Liang Y, Lv X and Frauenheim T 2022 Carrier doping-induced strong magnetoelastic coupling in 2D lattice *Nanoscale* **14** 6718–21
- [8] Zaeimbashi M *et al* 2021 Ultra-compact dual-band smart NEMS magnetolectric antennas for simultaneous wireless energy harvesting and magnetic field sensing *Nat. Commun.* **12** 1–11 (<https://nature.com/articles/s41467-021-23256-z>)
- [9] Liu H, Ye Y, Zhang X, Yang T, Wen W and Jiang S 2022 Ferroelectricity in organic materials: from materials characteristics to de novo design *J. Mater Chem. C. Mater* **10** 13676–89
- [10] Pugazhvadivu K S, Balakrishnan L, Mohan Rao G and Tamilarasan K 2014 Room temperature ferromagnetic and ferroelectric properties of Bi_{1-x}Ca_xMnO₃ thin films *AIP Adv.* **4** 1–8

- [11] Choi E M, Kursumovic A, Lee O J, Kleibeuker J E, Chen A, Zhang W, Wang H and Macmanus-Driscoll J L 2014 Ferroelectric Sm-doped BiMnO₃ thin films with ferromagnetic transition temperature enhanced to 140 K *ACS Appl. Mater. Interfaces* **6** 14836–43
- [12] Mohamed W S, Nucara A, Calestani G, Mezzadri F, Gilioli E, Capitani F, Postorino P and Calvani P 2015 Optical study of the vibrational and dielectric properties of BiMnO₃ *Phys. Rev. B Condens. Matter Mater. Phys.* **92** 1–6
- [13] Rahangdale K K and Ganguly S 2021 Sintering effect on the structure and multiferroic behavior of nanostructured BiMnO₃ ceramic synthesized by mechanochemical route *Ferroelectrics* **585** 97–110
- [14] Zhong C, Fang J and Jiang Q 2004 Magnetodielectric effects in the ferroelectric ferromagnet BiMnO₃ *J. Phys. Condens. Matter* **16** 9059–68
- [15] De Luca G M, Preziosi D, Chiarella F, Di Capua R, Gariglio S, Lettieri S and Salluzzo M 2013 Ferromagnetism and ferroelectricity in epitaxial BiMnO₃ ultra-thin films *Appl. Phys. Lett.* **103** 1–4
- [16] Toulemonde P et al 2009 Single crystal growth of BiMnO₃ under high pressure-high temperature *High Press Res.* **29** 600–4
- [17] Umoh G V 2022 Synthesis of ferroelectric and multiferroics thin films of bimno3/ srtio3 and structural, piezoelectric, magnetic, optical, and mechanical properties characterization *PhD Thesis Cimav* 20–67 (<https://repositorioslatinoamericanos.uchile.cl/handle/2250/7728569>)
- [18] Umoh G V, Leal-Perez J E, Olive-Méndez S F, González-Hernández J, Mercader-Trejo F, Herrera-Basurto R, Auciello O and Hurtado-Macias A 2022 Complex dielectric function, cole-cole, and optical properties evaluation in BiMnO₃ thin-films by valence electron energy loss spectrometry (VEELS) analysis *Ceram. Int.* **48** 22182–7
- [19] Eliseev E A, Kalinin S V, Jesse S, Bravina S L and Morozovska A N 2007 Electromechanical detection in scanning probe microscopy: tip models and materials contrast *J. Appl. Phys.* **102** 1–12
- [20] Anon Sci-Hub | Switching spectroscopy piezoresponse force microscopy of ferroelectric materials *Appl. Phys. Lett.* **88** 062908 |
- [21] Brinckmann S and Schwaiger R 2021 Towards enhanced nanoindentation by image recognition *J. Mater. Res.* **36** 2266–76
- [22] Kim Y-J, Park H-S and Yang C-H 2021 Raman imaging of ferroelastically configurable jahn–teller domains in LaMnO₃ *npj Quantum Mater.* **6** 1–11
- [23] Naganuma H, Kovacs A, Harima T, Shima H, Okamura S and Hirotsu Y 2009 Structural analysis of interfacial strained epitaxial BiMnO₃ films fabricated by chemical solution deposition *J. Appl. Phys.* **105**
- [24] Shin H W and Son J Y 2019 Enhanced multiferroic properties of tetragonally strained epitaxial BiMnO₃ thin films grown on single crystal Rh substrates *Solid State Sci.* **91** 7–9
- [25] Toulemonde P, Bordet P, Bouvier P and Kreisel J 2014 Single-crystalline BiMnO₃ studied by temperature-dependent x-ray diffraction and raman spectroscopy *Phys. Rev. B Condens. Matter Mater. Phys.* **89** 1–6
- [26] Rani S, Sanghi S, Agarwal A, Kumar R and Singh O 2022 Crystal structure, magnetic and dielectric properties of Er-doped BiFeO₃ ceramics *Applied Physics A* **2022** 128:7 **128** 1–17
- [27] Goian V, Kamba S, Savinov M, Nuzhnyy D, Borodavka F, Vaněk P and Belik A A 2012 Absence of ferroelectricity in BiMnO₃ ceramics *J. Appl. Phys.* **112** 1–6
- [28] Elcoro L, Bradlyn B, Wang Z, Vergniory M G, Cano J, Felser C, Andrei Bernevig B, Orobengoa D, De La Flor G and Aroyo M I 2017 Double crystallographic groups and their representations on the bilbao crystallographic server *J. Appl. Crystallogr.* **50** 1457–77
- [29] Aroyo M I, Kirov A, Capillas C, Perez-Mato J M and Wondratschek H 2006 Foundations of crystallography bilbao crystallographic server. II. representations of crystallographic point groups and space groups *Acta Cryst* **62** 115–28
- [30] Haumont R, Kreisel J, Bouvier P and Hippert F 2006 Phonon anomalies and the ferroelectric phase transition in multiferroic BiFeO₃ *Phys. Rev. B Condens. Matter Mater. Phys.* **73** 1–7
- [31] Grizalez M, Mendoza G A and Prieto P 2009 Analysis of multiferroic properties in BiMnO₃ thin films *XIX Latin American Symposium on Solid State Physics (Bristol: Institute of Physics Publishing)* 167, 1–5 *Journal of Physics: Conference Series*
- [32] Pintilie L, Boldyreva K, Alexe M and Hesse D 2008 Coexistence of ferroelectricity and antiferroelectricity in epitaxial PbZrO₃ films with different orientations *J. Appl. Phys.* **103** 1–5
- [33] Ali Saha R, Halder A, Fu D, Itoh M, Saha-Dasgupta T and Ray S 2021 The critical role of stereochemically active lone pair in introducing high temperature ferroelectricity *Inorg. Chem.* **60** 4068–75
- [34] Jin C et al 2021 Super-flexible freestanding BiMnO₃ membranes with stable ferroelectricity and ferromagnetism *Adv. Sci.* **8** 1–9
- [35] Zhang H, De Luca F, Wang H, Mingard K and Gee M 2022 Deformation mechanism of WC single crystals under nanoindentation: Effects of surface defects and orientation on pop-in and hysteresis *Int. J. Refract. Metals Hard Mater* **106** 105850
- [36] Johnson K L 1989 *Contact Mechanics* **33** 1–20 (<https://scientific.net/KEM.33.17>)
- [37] Zhuo F, Eckstein U R, Khansur N H, Dietz C, Urushihara D, Asaka T, Kakimoto K ichi, Webber K G, Fang X and Rödel J 2022 Temperature-induced changes of the electrical and mechanical properties of aerosol-deposited BaTiO₃ thick films for energy storage applications *J. Am. Ceram. Soc.* **105** 4108–21
- [38] Scholz T, Schneider G A, Muñoz-Saldaña J and Swain M V 2004 Fracture toughness from submicron derived indentation cracks *Appl. Phys. Lett.* **84** 3055
- [39] Swain M V and Hagan J T 1976 Indentation plasticity and the ensuing fracture of glass *J. Phys. D: Appl. Phys.* **9** 2201–14
- [40] Domínguez-Ríos C, Hurtado-Macias A, Torres-Sánchez R, Ramos M A and González-Hernández J 2012 Measurement of mechanical properties of an electroless Ni-B coating using nanoindentation *Ind. Eng. Chem. Res.* **51** 7762–8
- [41] Li H and Chen J 2021 Determination of elastic moduli of elastic–plastic microspherical materials using nanoindentation simulation without mechanical polishing *Beilstein Journal of Nanotechnology* **12**:17 **12** 213–21
- [42] Juri A Z, Basak A K and Yin L 2022 In-situ SEM cyclic nanoindentation of pre-sintered and sintered zirconia materials *J. Mech. Behav. Biomed. Mater.* **126** 105068
- [43] Jha K K, Suksawang N, Lahiri D and Agarwal A 2013 Evaluating initial unloading stiffness from elastic work-of-indentation measured in a nanoindentation experiment *J. Mater. Res.* **28** 789–97
- [44] Schäufele A B and Härdtl K H 1996 Ferroelastic properties of lead zirconate titanate ceramics *J. Am. Ceram. Soc.* **79** 2637–40
- [45] Hwang S C, Lynch C S and McMeeking R M 1995 Ferroelectric/ferroelastic interactions and a polarization switching model *Acta Metall. Mater.* **43** 2073–84